

METHODS

Experimental Methods

The experiments described were carried out at the W. M. Keck Research Laboratory in Astrochemistry.¹⁻³ The apparatus is housed in a hydrocarbon-free stainless steel ultra-high vacuum (UHV) chamber which is maintained at a few 10^{-11} Torr by magnetically levitated turbomolecular pumps.⁴ A closed cycle helium refrigerator (Sumitomo Heavy Industries, RDK-415E) cools a mirror-polished silver wafer (15.1×12.6 or 32.8×32.8 mm for PI-ReToF-MS or FTIR-TPD experiments, respectively) to 5 – 12 K. The refrigerator-wafer assembly is rotatable about the vertical axis because it is mounted on a doubly differentially pumped rotatable flange (Thermionics Vacuum Products, RNN-600/FA/MCO), and can be translated along its rotation axis via an adjustable bellows (McAllister, BLT106). Ices were prepared by passing ammonia gas (NH_3 , Matheson, 99.99%) and acetaldehyde vapor (acetaldehyde Sigma Aldrich, anhydrous 99.5 %; acetaldehyde- d_3 , Sigma Aldrich, ≥ 98 % purity, ≥ 98 atom % D; acetaldehyde- d_4 , Sigma Aldrich, 99 % purity, ≥ 98 atom % D; acetaldehyde- $^{13}\text{C}_2$, Sigma Aldrich, 99 atom % ^{13}C) through separate glass capillary arrays (10 or 25.4 mm diameter for PI-ReToF-MS or FTIR-TPD experiments, respectively) directed at the cooled wafer. Partial pressures of each ice component were adjusted by the use of leak valves to achieve approximately a 2:1 ratio of [ammonia]:[acetaldehyde]. Ice thickness was determined by monitoring the ice deposition with a helium-neon laser (CVI Melles-Griot, 25-LHP-230, 632.8 nm) at a 4° angle of incidence and measuring variations in reflected power due to thin film interference by the ice.⁵ The index of refraction of the mixed ice is unknown though it is necessary to determine ice thickness from interferometric measurements. This parameter was approximated by the average of the indexes of refraction of the two components, 1.33 for ammonia at 18 K and 1.303 at 15 K for acetaldehyde, with an average of 1.32 ± 0.02 .^{6,7} Details of the composition and thickness of ices studied are reported in Table S1

Fourier transform infrared (FTIR) spectra (Thermo Electron, Nicolet 6700) were measured in the range $6000 - 500 \text{ cm}^{-1}$ with 230 spectra averaged over a two-minute period after ice deposition and used to calculate the relative abundance of the two components (Figures S1 – S4, Table S2). Relative concentrations of ammonia and acetaldehyde in ices were determined using integrated infrared absorption strength of the components. For ammonia, the integrated intensities of ν_2 , ν_3 , and ν_4 observed at 1077 , 3394 , and 1627 cm^{-1} have absorption coefficients of 2.1×10^{-17} , $2.3 \times$

10^{-17} , and 5.6×10^{-18} cm molec. $^{-1}$, respectively.⁸ For acetaldehyde, the integrated intensities of ν_1 , ν_5 , ν_7 , and ν_8 observed at 3006, 1428, 1350, and 1128 cm $^{-1}$ have absorption coefficients of 5.1×10^{-19} , 1.9×10^{-18} , 1.1×10^{-18} , and 6.6×10^{-19} cm molec. $^{-1}$, respectively.⁹ Temperature programmed desorption (TPD) was conducted using a ramp of 1 K min $^{-1}$, during which FTIR spectra were measured every 2 minutes until the ice had completely sublimed.

The photoionization reflectron time-of-flight mass spectrometry (PI-ReToF-MS) technique has been discussed in detail elsewhere.¹ Ices were heated to 320 K with temperature programmed desorption (TPD) at a rate of 1 K min $^{-1}$. During TPD, pulsed 30 Hz coherent vacuum ultraviolet (VUV) light was passed 1 – 2 mm above the surface of the ice to photoionize subliming molecules. VUV light was produced via both degenerate ($\omega_{\text{VUV}} = 3\omega_1$) and resonant difference four-wave mixing ($\omega_{\text{VUV}} = 2\omega_1 - \omega_2$) schemes (Table S4). Four-wave mixing (ω_1 ; dye laser, Sirah Lasertechnik, Cobra-Stretch) two-photon absorption of Xenon and 1064 nm (ω_2 ; Nd:YAG laser, Spectra-Physics, Quanta Ray PRO 270-30) was used to produce 11.10 eV photons. Difference frequency generation ($2\omega_1 - \omega_2$) with 202.3 nm (ω_1) and a second dye laser operating at 730.8 or 490.7 nm (ω_2) produced photons at 10.56 or 9.73 eV, respectively. Alternatively, exploiting the same two-photon absorption and Nd:YAG harmonics at 532 or 355 nm produced photons of 9.93, or 8.76 eV. After generation of the selected ω_1 and ω_2 , the lasers were made collinear and directed through a lens (Thorlabs, LA5479, $f = 300$ mm) and focused into a jet of rare gas in the VUV generation vacuum chamber. Coherent VUV light exiting this chamber was separated from ω_1 and ω_2 by passing the collinear beams through an off-axis lithium fluoride (LiF) biconvex lens (Korth Kristalle, $R_1 = R_2 = 131.22$ mm) which imparts an angular separation between the three frequencies and directs only the VUV light through an aperture to the ionization region. Ions formed are mass-analyzed in a reflectron time-of-flight mass spectrometer (ReToF-MS; Jordan TOF Products) and detected with a dual microchannel plate (MCP) detector in the chevron configuration (Jordan TOF Products). MCP signal was amplified (Ortec, 9305) before discrimination and amplification to 4 V (Advanced Research Instruments Corp., F100-TD) and ultimately recorded by a multichannel scaler (FAST ComTec, MCS6A) interfaced to a personal computer. Ion arrival times were recorded to 3.2 ns accuracy, mass spectra were repeated at a rate of 30 Hz, and new mass spectra were accumulated every two minutes during TPD until the temperature of the sample reached 320 K.

Computational Methods

Computation of Adiabatic Ionization Energy

Geometries of neutral molecules were optimized for all possible combinations of dihedral angles of asymmetric internal rotors –OH and –NH₂, and *E/Z* configurations about C=N bonds. For ions, starting geometries for optimization were the optimized neutral molecules. These calculations used the CBS-QB3 composite method implemented in the GAUSSIAN 09 program package,¹⁰ and is characterized by mean absolute error of 4.52 kJ mol⁻¹ and root-mean-square error of 6.32 kJ mol⁻¹ for computed enthalpies of formation for the G2/97 test set.^{11,12} Optimized molecular structures arrived at with this method provide accuracy 0.01 – 0.02 Å for bond lengths as well as 1 – 2° for bond angles. This method also has a mean absolute error of 0.05 eV for computed adiabatic ionization energies, which has been applied as ± 0.05 eV to all conformer specific ionization energies that form the ranges presented in Figure 1.

Computation of Potential Energy Surfaces (PES)

Potential energy surfaces for the reactions of ammonia and acetaldehyde in mixed ices were computed using the ωB97X-D density functional¹³ with the 6-311G(d,p) basis set. Implicit solvent effects were taken into account by applying the universal continuum SCRF SMD model.¹⁴ First, geometry optimization and calculation of vibrational frequencies were carried out using the parameters of liquid ammonia as solvent (dielectric constant 22.63, square of the index of refraction at optical frequencies 1.76).¹⁵ To verify the sensitivity of the energetics with respect to the parameters of solvent in the SCRF SMD calculations we performed single-point calculations with parameters of solid ammonia below the freezing temperature of 77 K (dielectric constant 3.4, square of the index of refraction at optical frequencies 1.96).¹⁶ This resulted only in minor changes of relative energies along the reaction pathways.

Geometries of coordination complexes of metal ions with water and 1-(1-hydroxyethylamino)ethanol **3** were optimized at the ωB97X-D/6-311++G(d,p) level of theory. The same method was employed for computing vibrational frequencies of the complexes and also their zero-point vibrational energies, entropies, and thermal Gibbs free energies at 298.15 K. Finally, the solvation effect in aqueous solution was evaluated using SCRF SMD calculations using Truhlar's M06-2X density functional¹⁷ with Dunning's cc-pVTZ basis set.¹⁸ The choice of this particular method here is due to the fact that the SMD approach for modeling aqueous solutions

was parametrized at the M06-2X/cc-pVTZ level.¹⁴ Gibbs free energy of the chelation reactions of the metal ions were further corrected for the change in the standard state from gaseous H₂O to water molecule in aqueous solution (8 kJ mol⁻¹ per each H₂O molecule released in the reaction) as recommended by Bryantsev et al.¹⁹

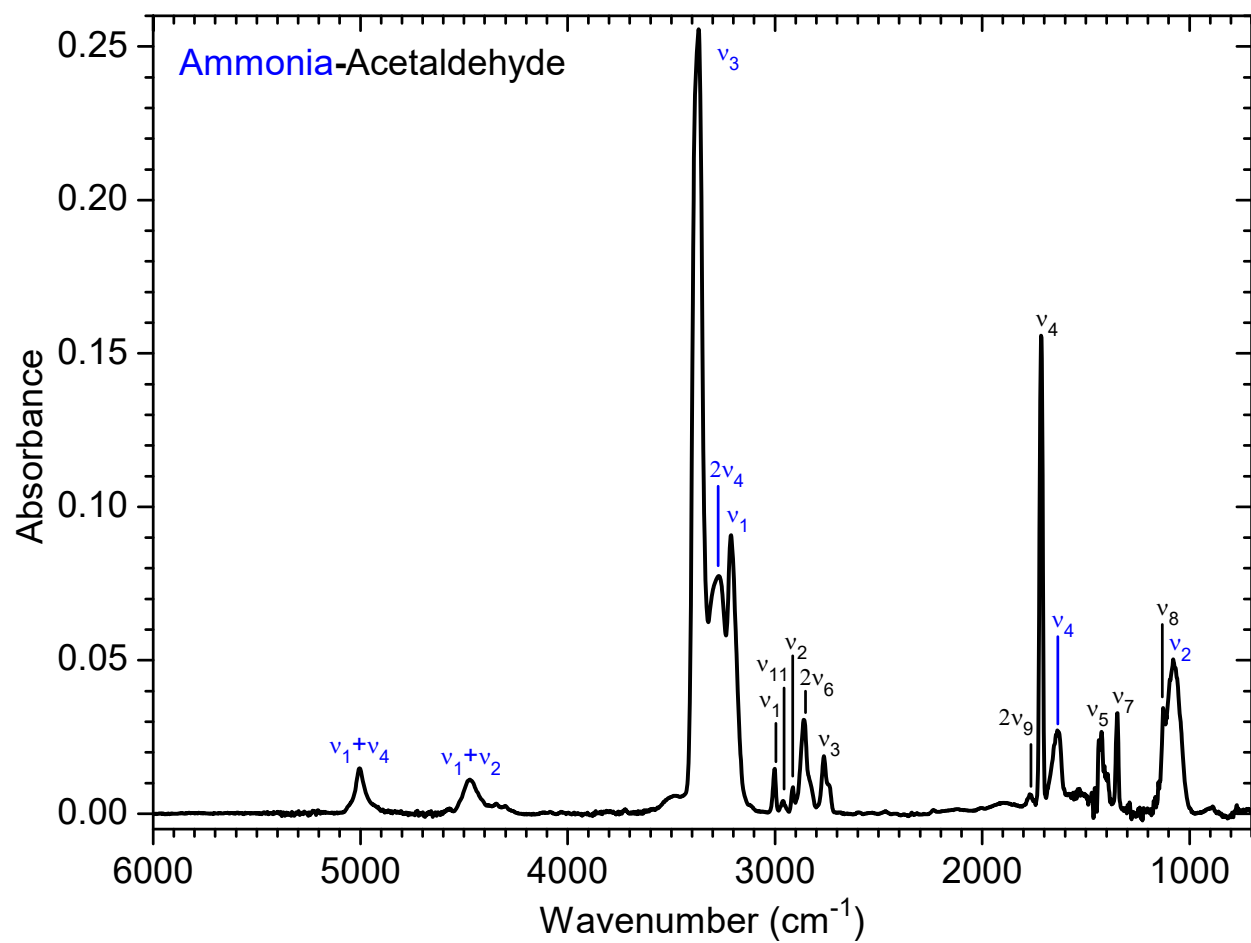


Figure S1. Infrared spectrum of ammonia–acetaldehyde ice measured immediately after deposition at 5 K.

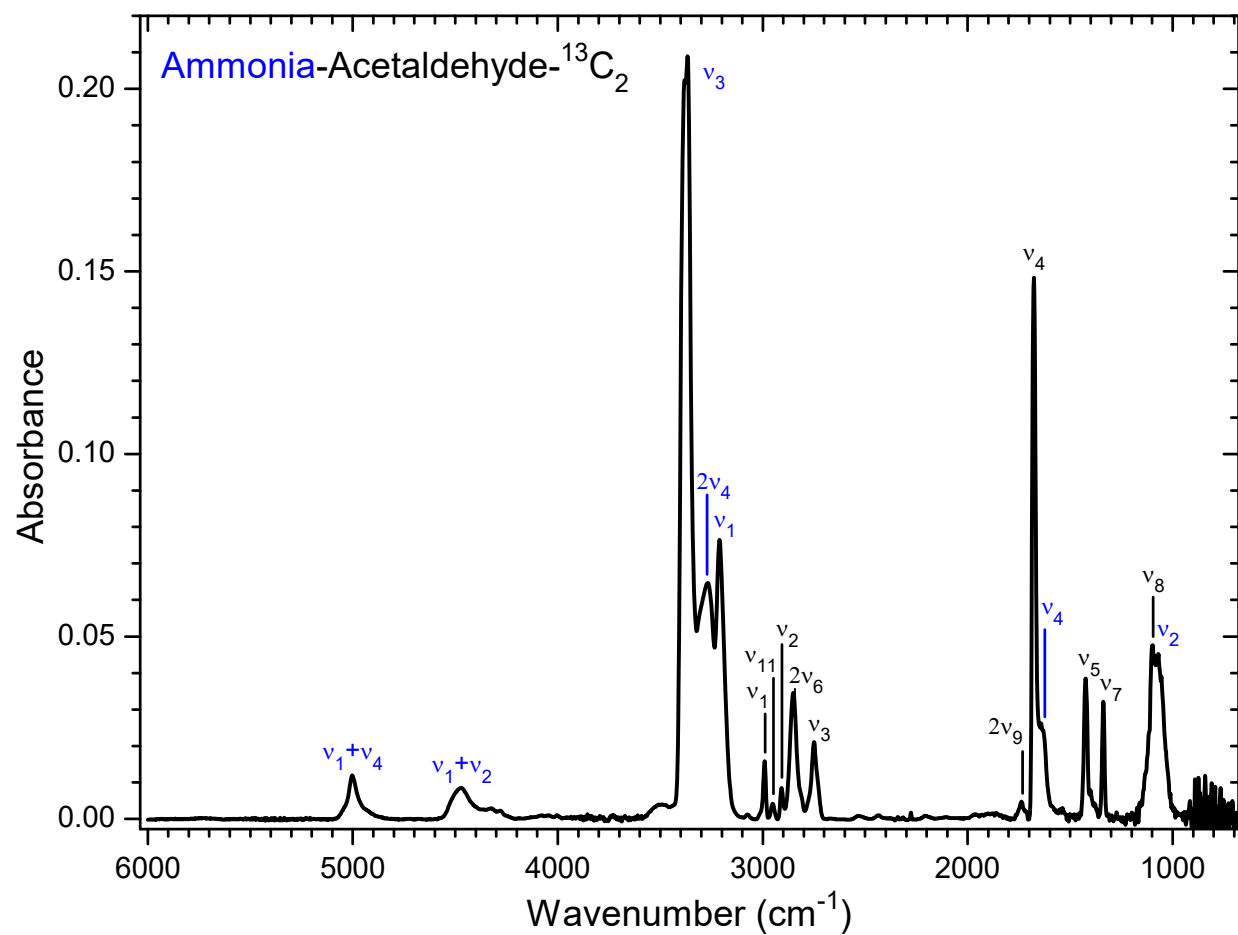


Figure S2. Infrared spectrum of ammonia–acetaldehyde-¹³C₂ ice measured immediately after deposition at 5 K.

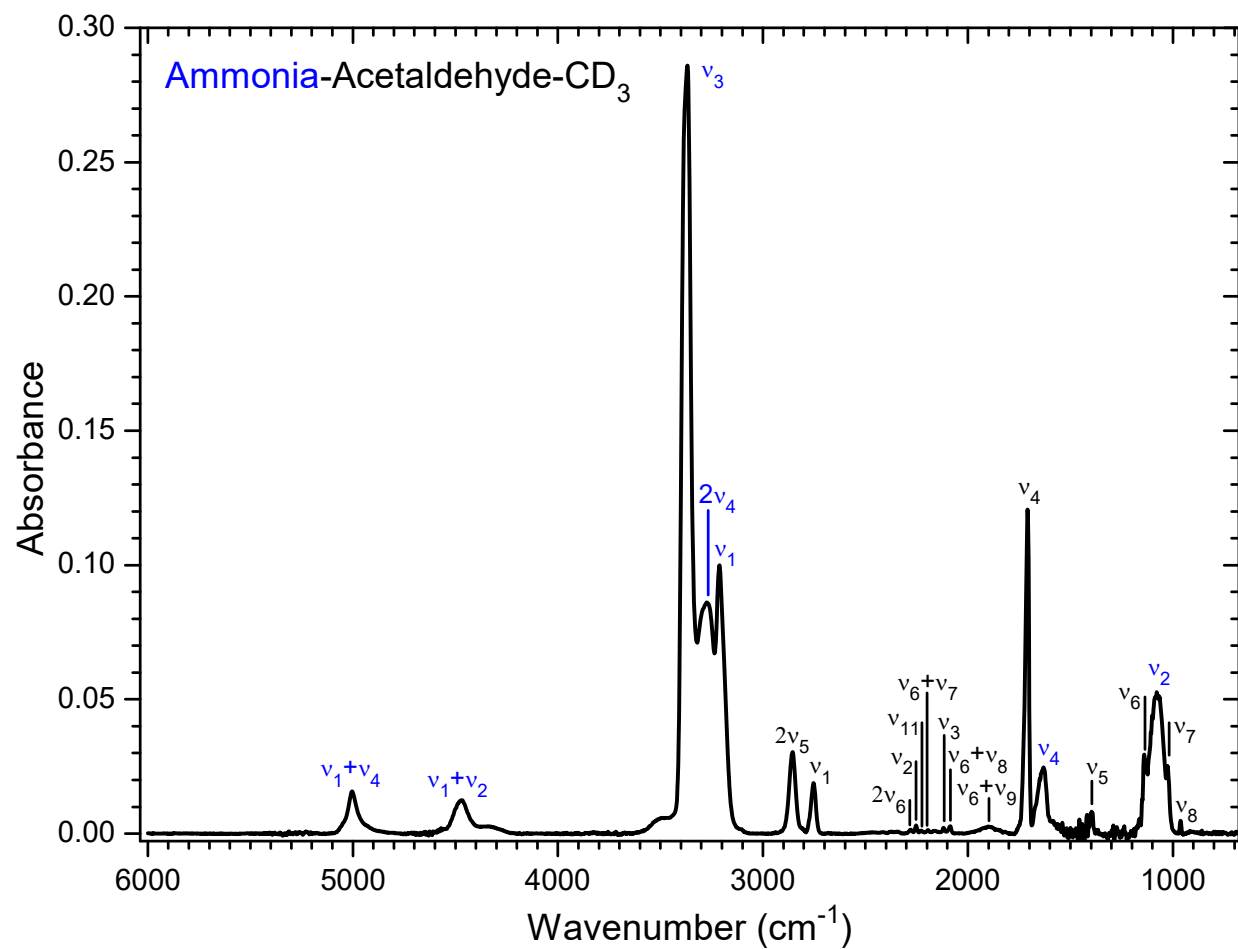


Figure S3. Infrared spectrum of ammonia–acetaldehyde-d₃ ice measured immediately after deposition at 5 K.

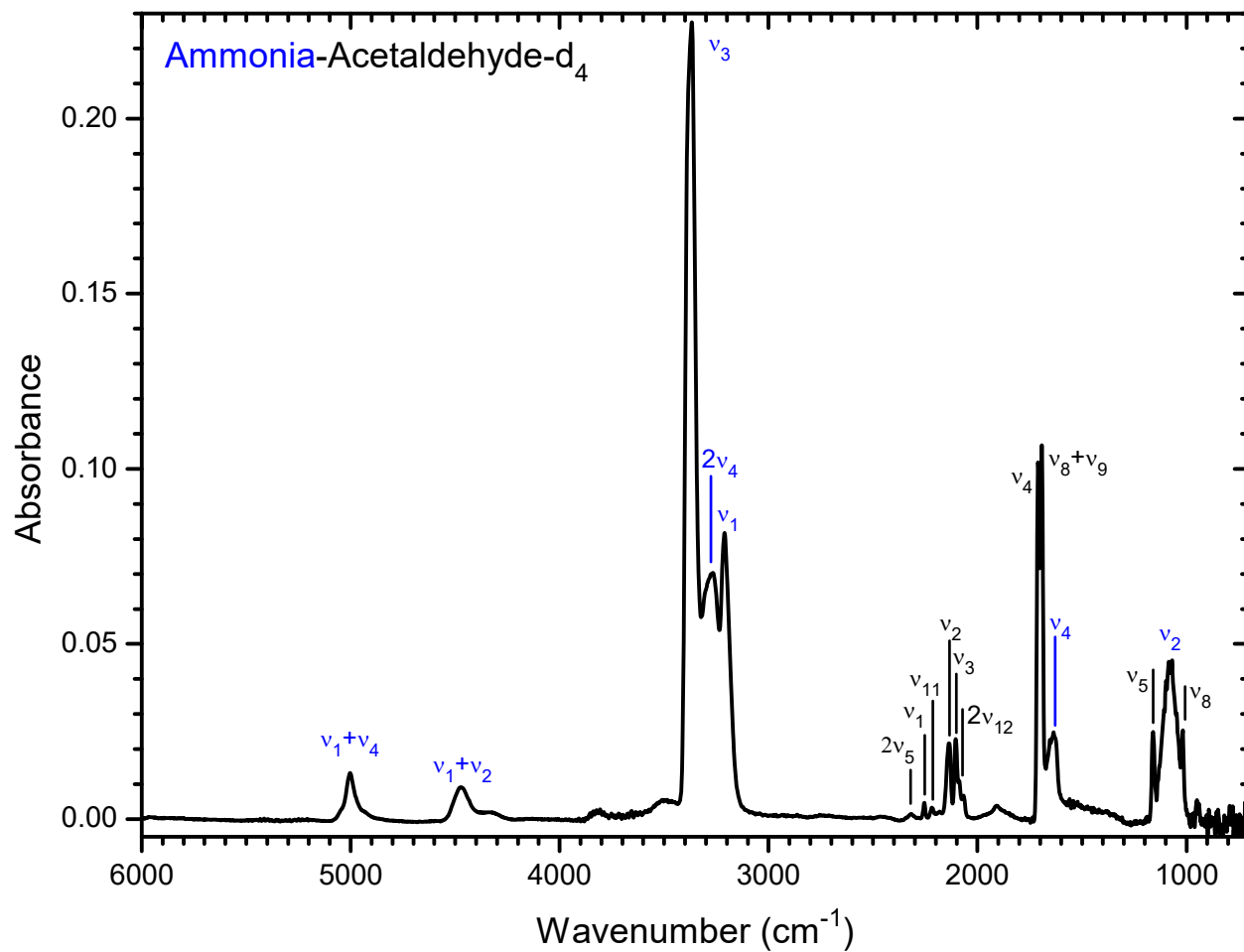


Figure S4. Infrared spectrum of ammonia–acetaldehyde-d₄ ice measured immediately after deposition at 5 K.

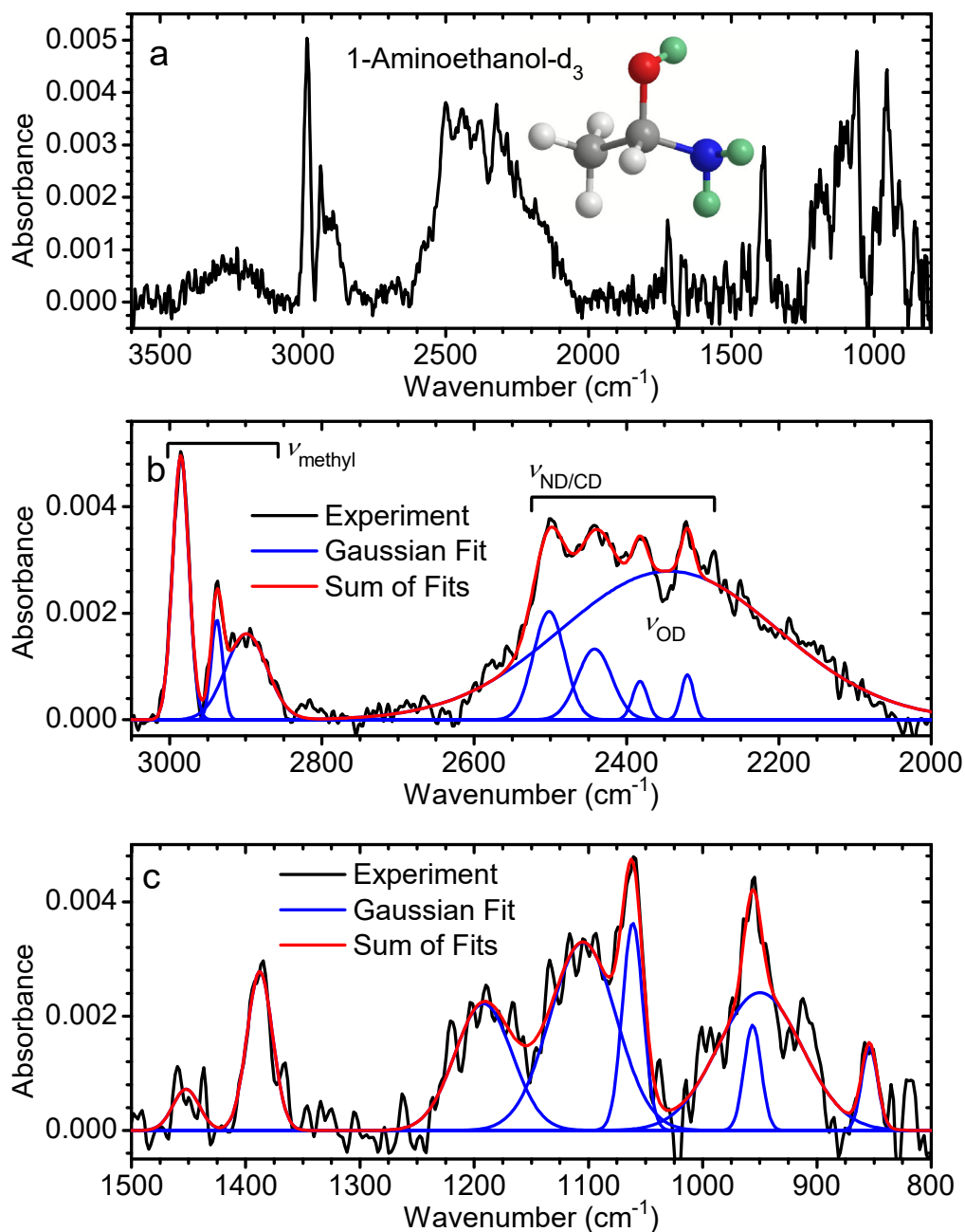


Figure S5. FTIR spectrum of acetaldehyde–ammonia-d₃ ice. (a) measured after sublimation of acetaldehyde and ammonia-d₃, (b) The region 3100 – 2000 cm⁻¹, comprising CH, CD, ND, and OD stretching modes, is shown magnified and deconvoluted, and (c) the region 1500 – 800 cm⁻¹, comprising CH, CD, ND, and OD bending modes in addition to CO, CC, and CN stretching modes, is also shown magnified and deconvoluted.

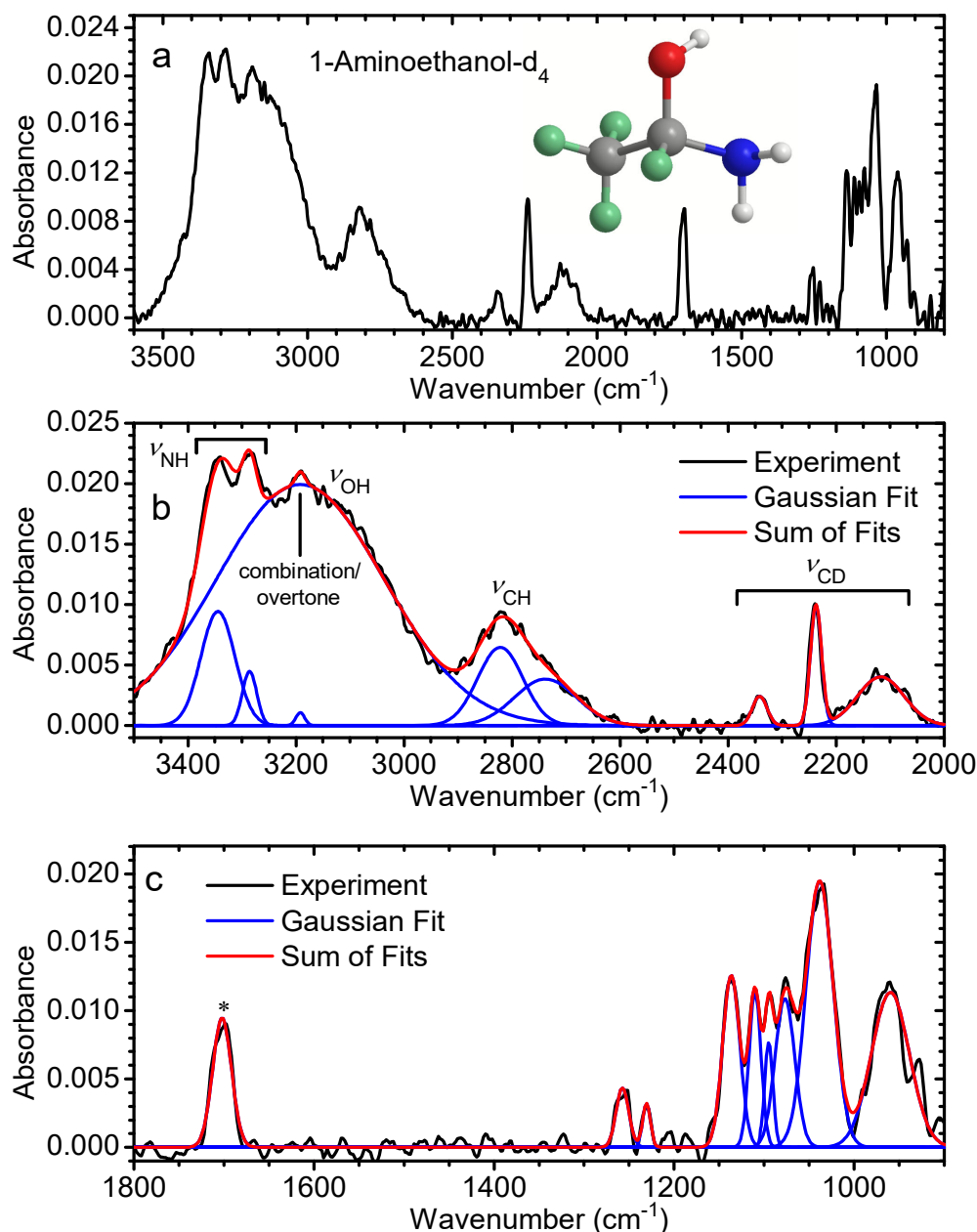


Figure S6. FTIR spectrum of acetaldehyde-d₄-ammonia ice. (a) measured after sublimation of acetaldehyde-d₄ and ammonia (b) The region 3500 – 2000 cm⁻¹, comprising NH, OH, CH, and CD stretching modes, is shown magnified and deconvoluted. (c) The region 1800 – 800 cm⁻¹, comprising NH, OH, CH, and CD bending modes in addition to CO, CC, and CN stretching modes, is also shown magnified and deconvoluted. The * marks the position of the CO stretch of acetaldehyde-d₄ which did not sublime completely.

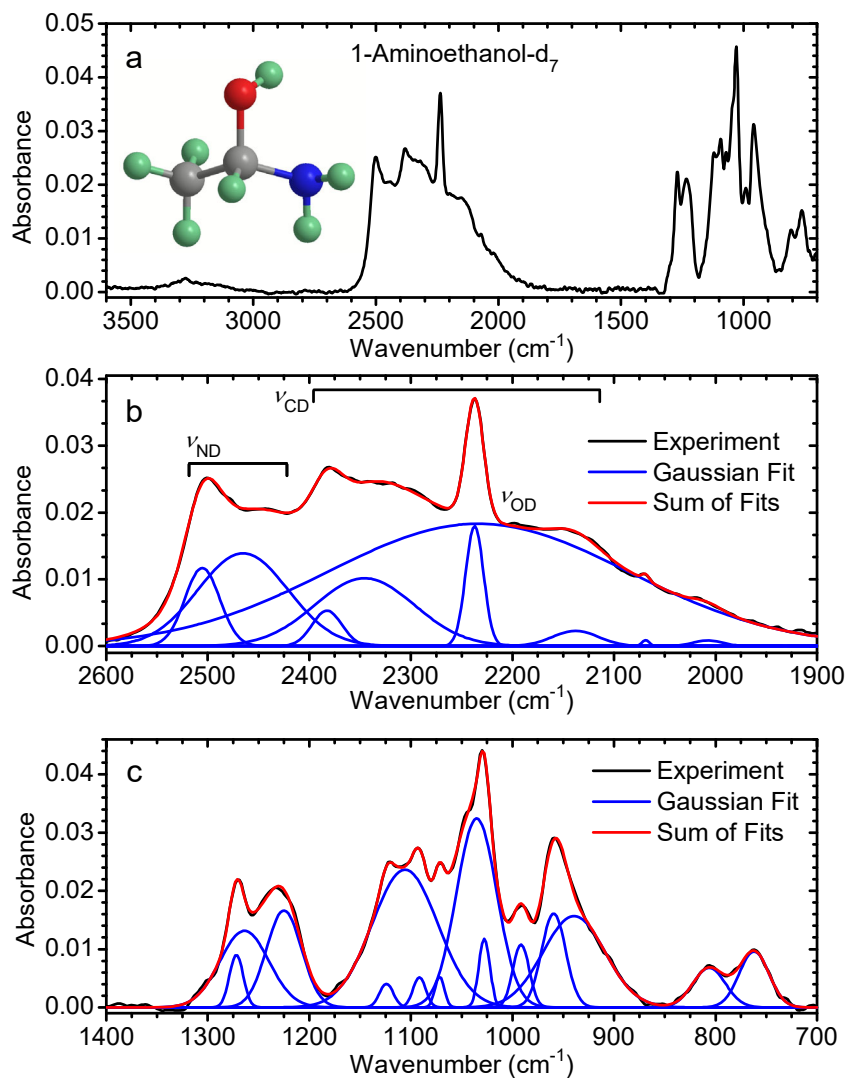


Figure S7. FTIR spectrum of acetaldehyde-d₄–ammonia-d₃ ice. (a) measured after sublimation of acetaldehyde-d₄ and ammonia-d₃ (b) The region 2600 – 1900 cm⁻¹, comprising ND, OD, and CD stretching modes, is shown magnified and deconvoluted. (c) The region 1400 – 700 cm⁻¹, comprising ND, OD, and CD bending modes in addition to CO, CC, and CN stretching modes, is also shown magnified and deconvoluted.

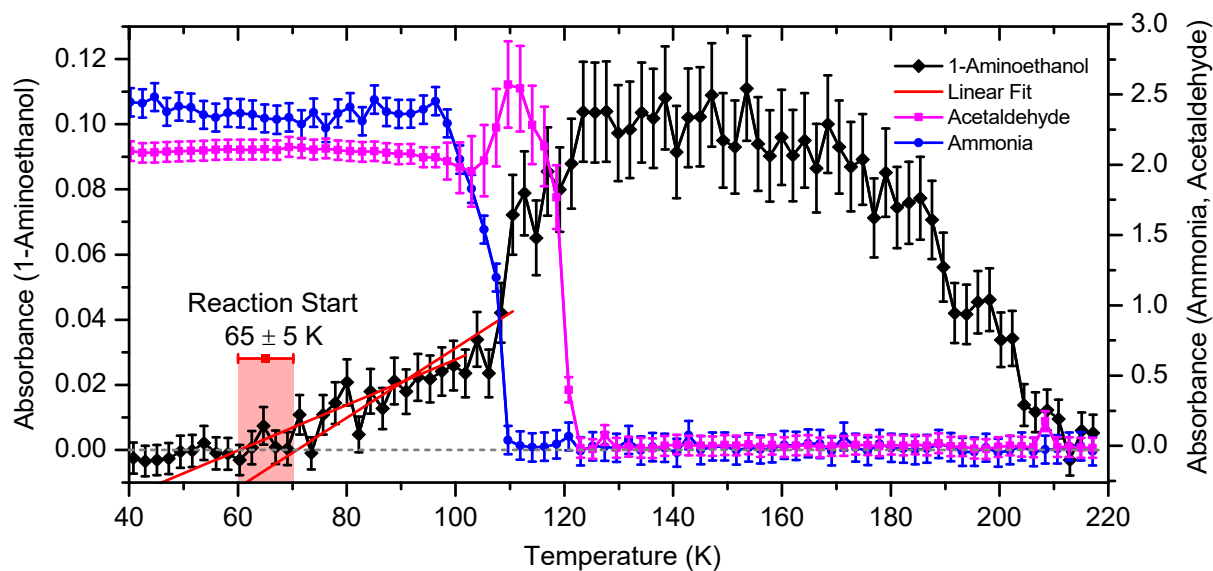


Figure S8. Integrated infrared absorption intensity of selected peaks of 1-aminoethanol (1176 cm^{-1} , $\nu_{\text{CO}}/\nu_{\text{CN}}/\nu_{\text{CC}}$), acetaldehyde (1716 cm^{-1} , ν_4), and ammonia (5003 cm^{-1} , $\nu_1 + \nu_4$). The onset of 1-aminoethanol formation is interpolated by fitting its absorption in the ranges of 60 – 100 K and 70 – 110 K to detailed view in inset.

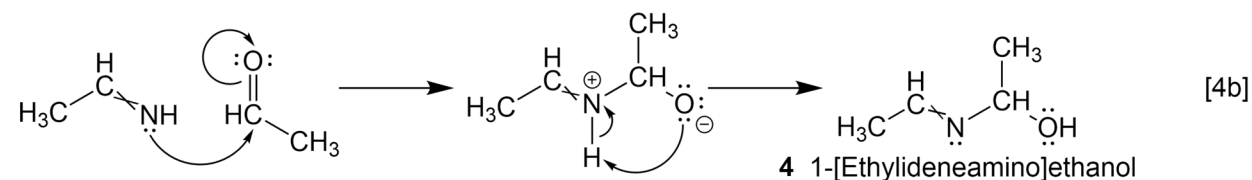
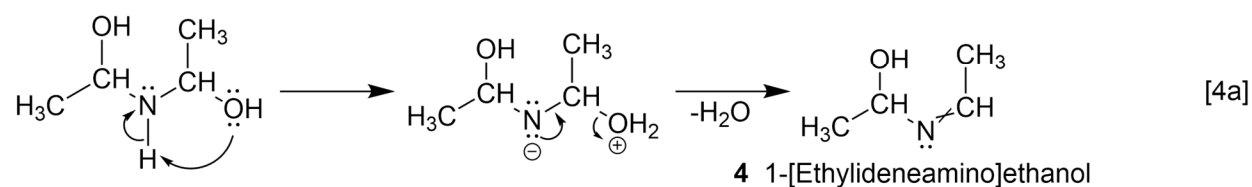
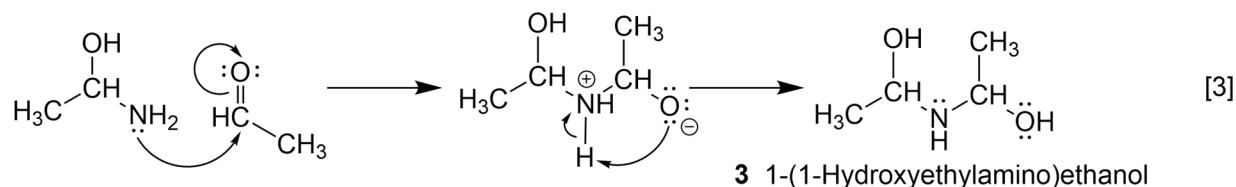
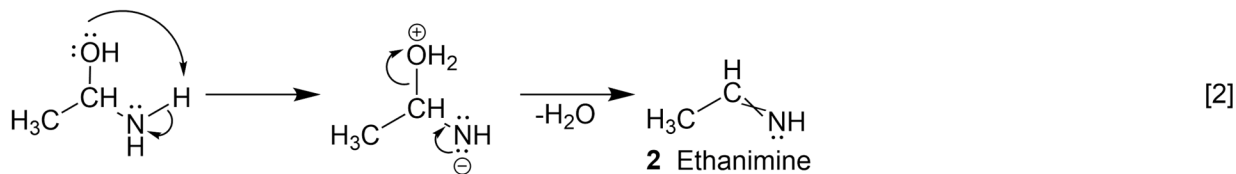
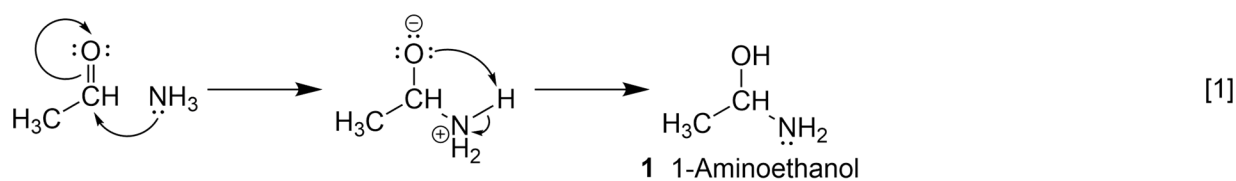


Figure S9. Mechanisms for nucleophilic addition of ammonia to acetaldehyde to form 1-aminoethanol (1). in reaction [1] and its subsequent dehydration in reaction [2] to complete a S_N2 (two-step nucleophilic substitution) synthesis of ethanimine (2). Addition of 1-aminoethanol (1) to acetaldehyde in reaction [3] followed by dehydration in reaction [4a] is one formation pathway to *E* or *Z* isomers of 1-ethylideneaminoethanol (4), and reaction [4b] shows a second pathway to this product in the addition of ethanimine (2) to acetaldehyde.

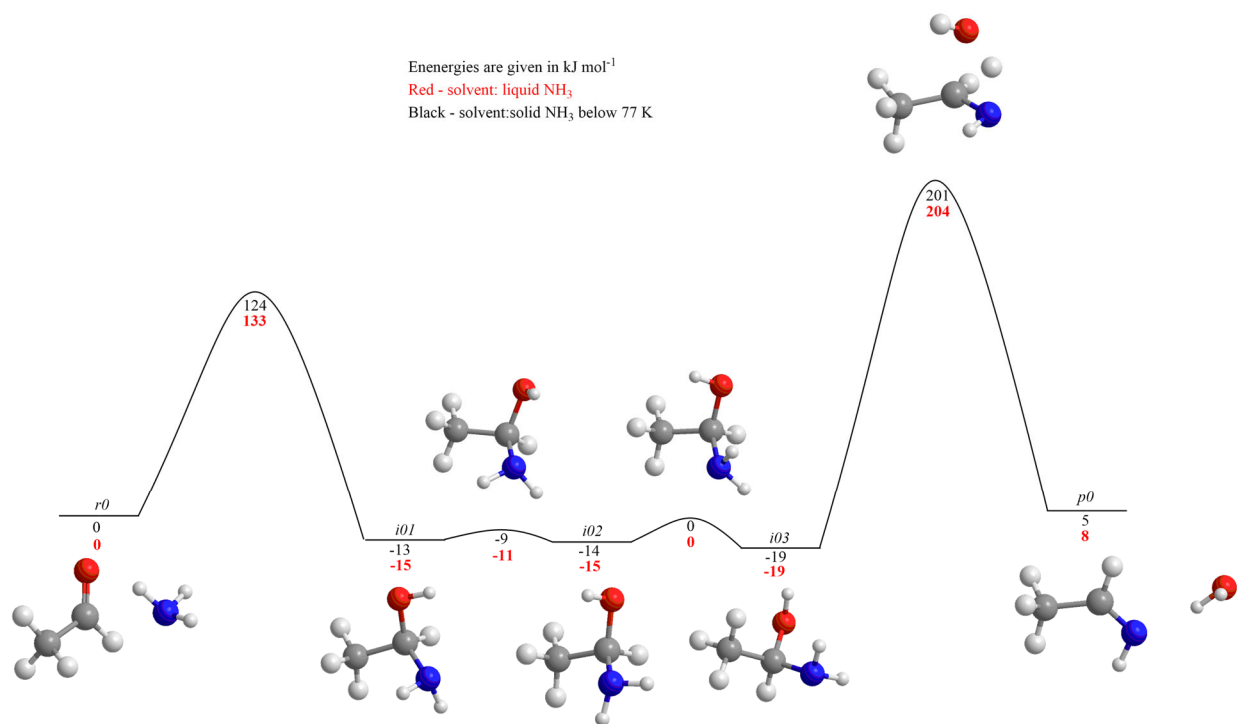


Figure S10. Potential energy surface for addition of ammonia to acetaldehyde. The energies (kJ mol⁻¹) are calculated at the ω B97X-D/6-311G(d,p) level of theory with zero-point corrections including ammonia as an implicit solvent within the SCRf SMD model. Red and black numbers respectively show relative energies computed using the parameters of liquid NH₃ as the solvent at 200 K and of solid NH₃ as a solvent below the freezing temperature of 77 K.

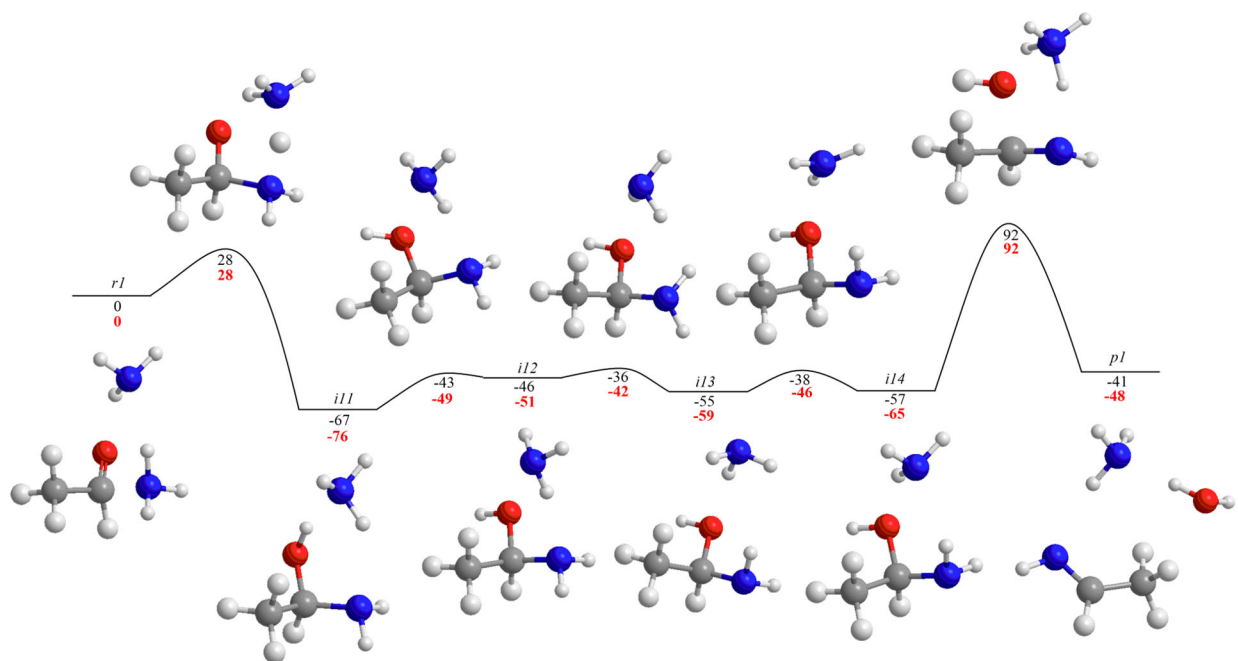


Figure S11. Potential energy surface for addition of ammonia to acetaldehyde with the incorporation of one microsolvating ammonia. Relative energies (kJ mol⁻¹) are calculated at the ω B97X-D/6-311G(d,p) level of theory including zero-point corrections including ammonia as an implicit solvent within the SCRF SMD model. Red and black numbers respectively show relative energies calculated using the parameters of liquid NH₃ as the solvent at 200 K and of solid NH₃ as a solvent below the freezing temperature of 77 K.

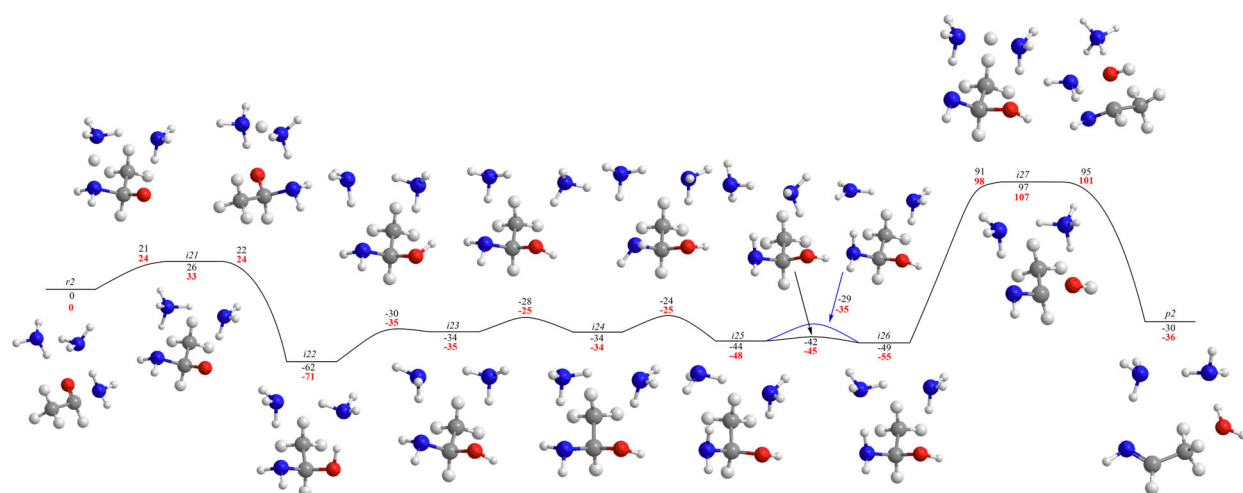


Figure S12. Potential energy surface for addition of ammonia to acetaldehyde with the incorporation of two microsolvating ammonia molecules. with relative energies (kJ mol⁻¹) given in kJ mol⁻¹. Relative energies are calculated at the ω B97X-D/6-311G(d,p) level of theory including zero-point corrections including ammonia as an implicit solvent within the SCRf SMD model. Red and black numbers respectively show relative energies calculated using the parameters of liquid NH₃ as the solvent at 200 K and of solid NH₃ as a solvent below the freezing temperature of 77 K.

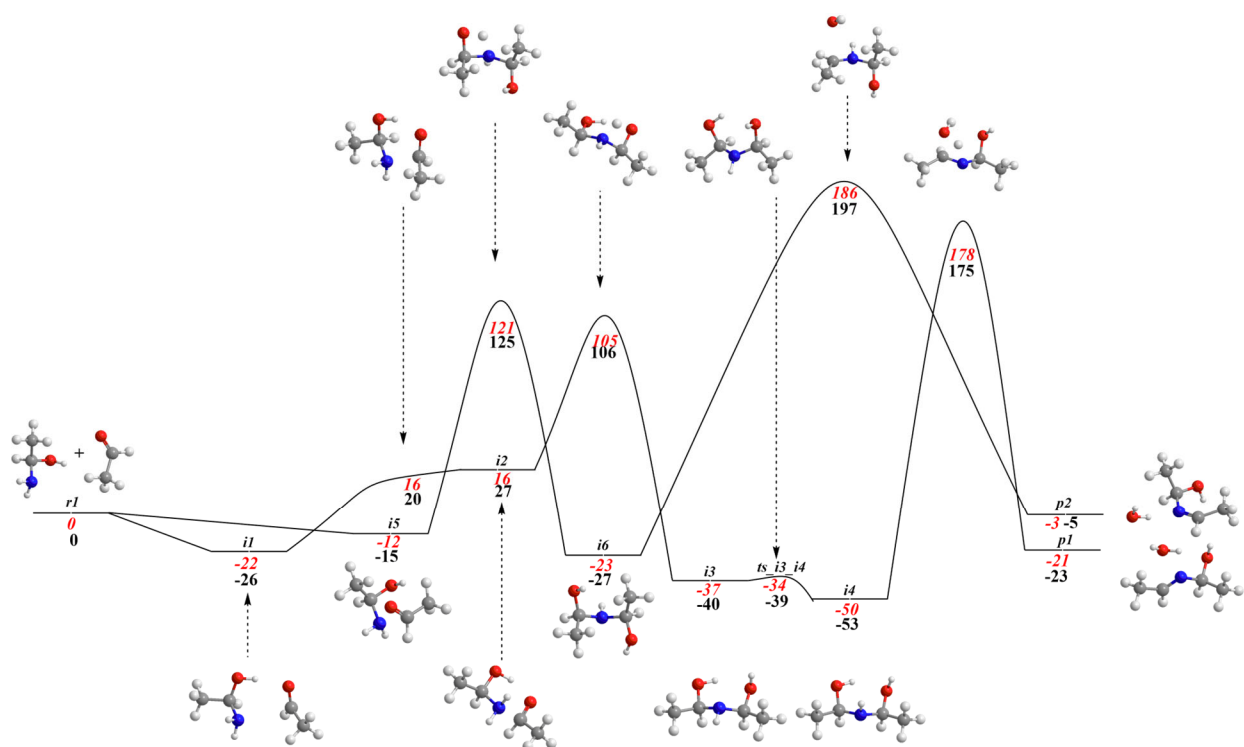


Figure S13. Potential energy surface for addition of 1-aminopropan-2-ol (1) to acetaldehyde.

Relative energies (kJ mol⁻¹) are calculated at the ω B97X-D/6-311G(d,p) level of theory including zero-point corrections including ammonia as an implicit solvent within the SCRF SMD model. Red and black numbers respectively show relative energies calculated using the parameters of liquid NH₃ as the solvent at 200 K and of solid NH₃ as a solvent below the freezing temperature of 77 K.

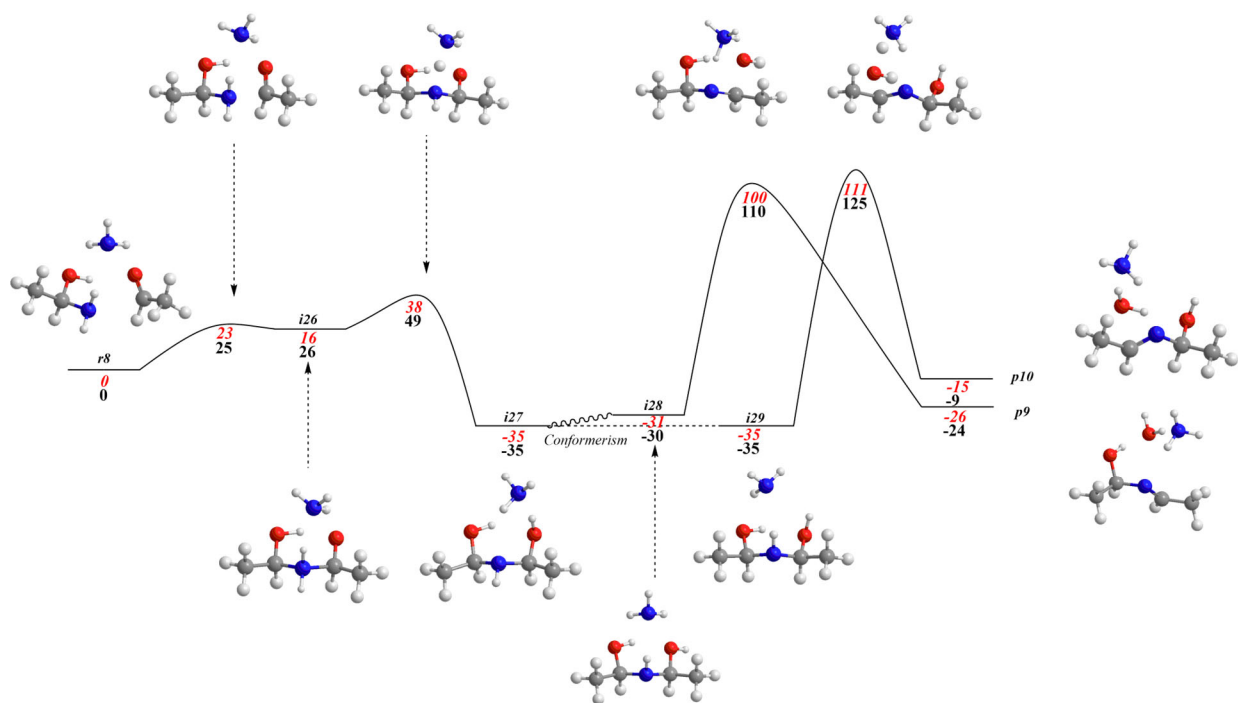


Figure S14. Potential energy surface for addition of 1-amoniethanol (1) to acetaldehyde with the incorporation of a microsolvating ammonia. Relative energies (kJ mol⁻¹) are calculated at the ω B97X-D/6-311G(d,p) level of theory including zero-point corrections including ammonia as an implicit solvent within the SCRF SMD model. Red and black numbers respectively show relative energies calculated using the parameters of liquid NH₃ as the solvent at 200 K and of solid NH₃ as a solvent below the freezing temperature of 77 K.

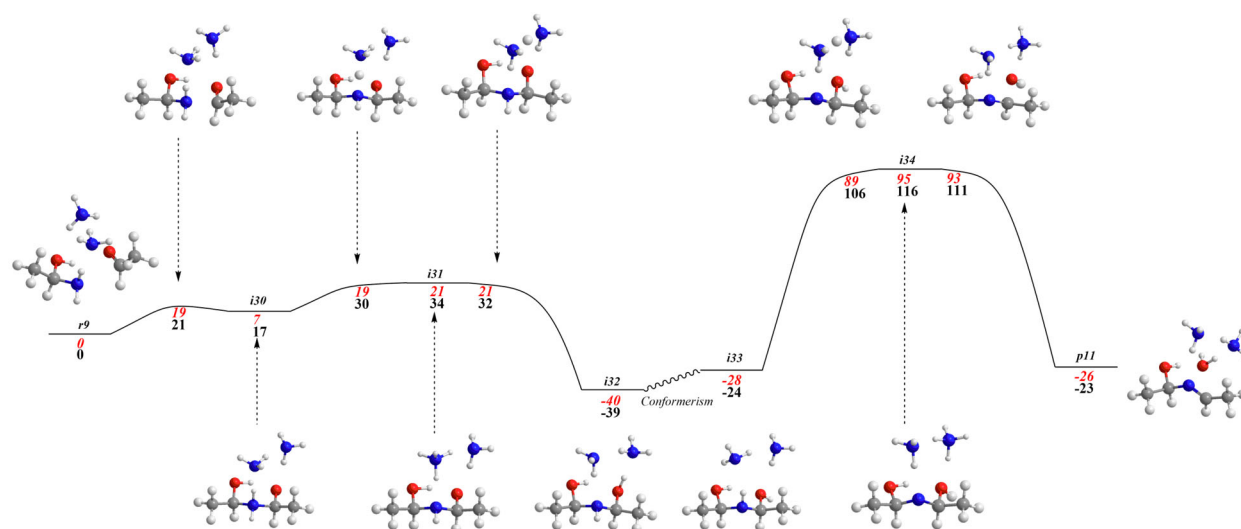


Figure S15. Potential energy surface for addition of 1-aminopropan-2-ol (1) to acetaldehyde with the incorporation of two microsolvent ammonia molecules. Relative energies (kJ mol⁻¹) are calculated at the ω B97X-D/6-311G(d,p) level of theory including zero-point corrections including ammonia as an implicit solvent within the SCRF SMD model. Red and black numbers respectively show relative energies calculated using the parameters of liquid NH₃ as the solvent at 200 K and of solid NH₃ as a solvent below the freezing temperature of 77 K.

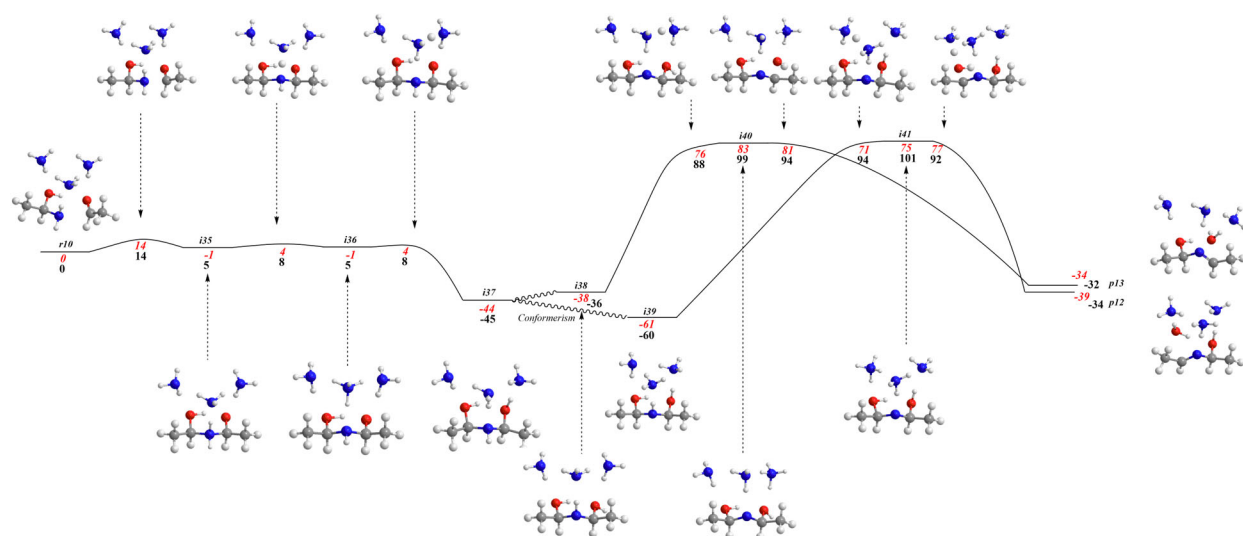


Figure S16. Potential energy surface for addition of 1-aminopropan-2-ol (1) to acetaldehyde with the incorporation of three microsolvent ammonia molecules. Relative energies (kJ mol⁻¹) are calculated at the ω B97X-D/6-311G(d,p) level of theory including zero-point corrections including ammonia as an implicit solvent within the SCRF SMD model. Red and black numbers respectively show relative energies calculated using the parameters of liquid NH₃ as the solvent at 200 K and of solid NH₃ as a solvent below the freezing temperature of 77 K.

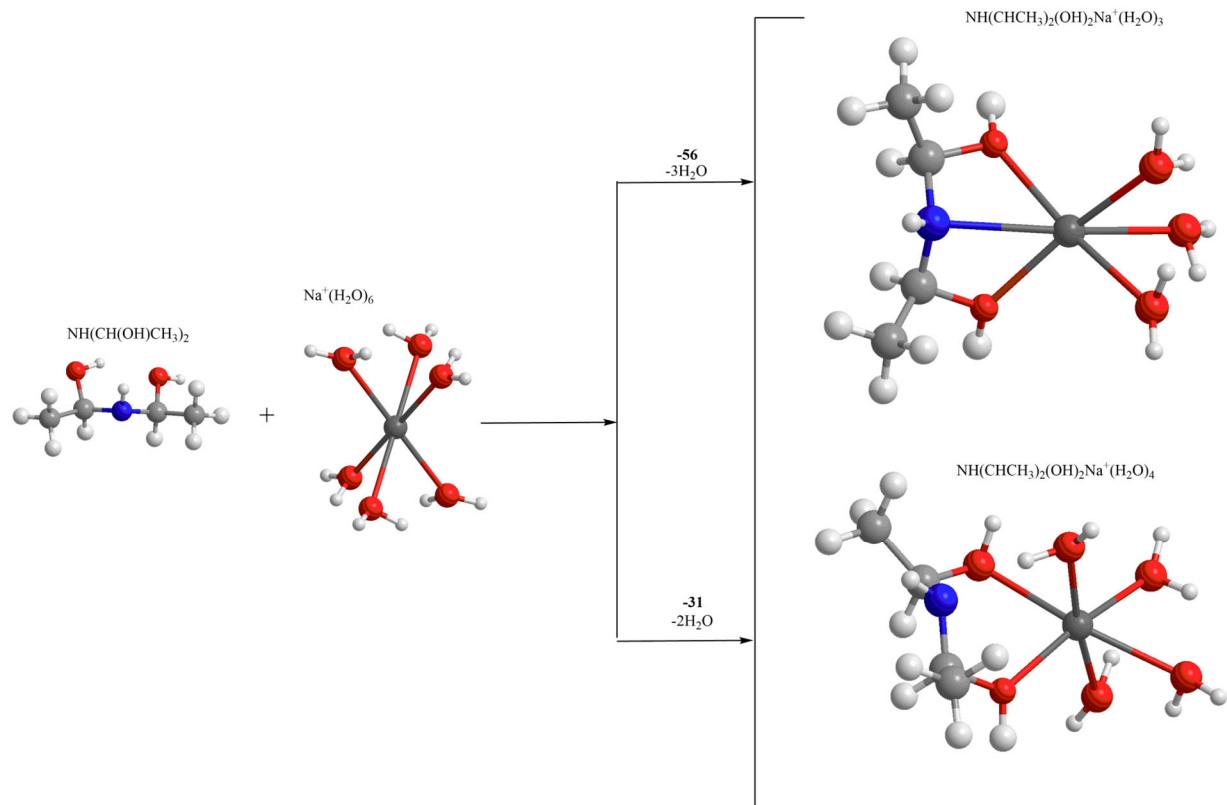


Figure S17. Free energies of reaction for Na^+ chelation by 1-(1-hydroxyethylamino)ethanol (3). Energies of substitution for two or three water ligands for 1-(1-hydroxyethylamino)ethanol (3) binding to Na^+ were calculated at the $\omega\text{B97X-D/6-311G(d,p)}$ level employing SCRF SMD modeling in aqueous solution at 298.15 K.

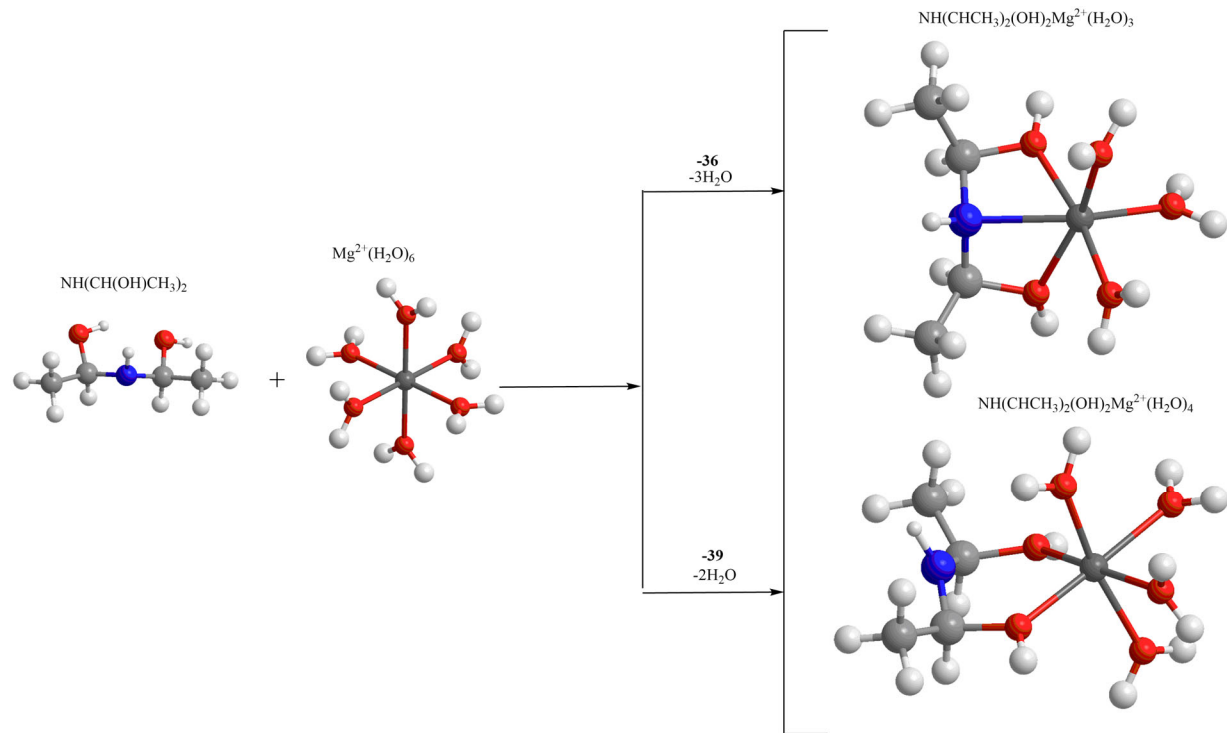


Figure S18. Free energies of reaction for Mg^{2+} chelation by 1-(1-hydroxyethylamino)ethanol (3**).** Energies of substitution for substitution of two or three water ligands for 1-(1-hydroxyethylamino)ethanol (**3**) binding to Mg^{2+} were calculated at the $\omega\text{B97X-D/6-311G(d,p)}$ level employing SCRF SMD modeling in aqueous solution at 298.15 K.

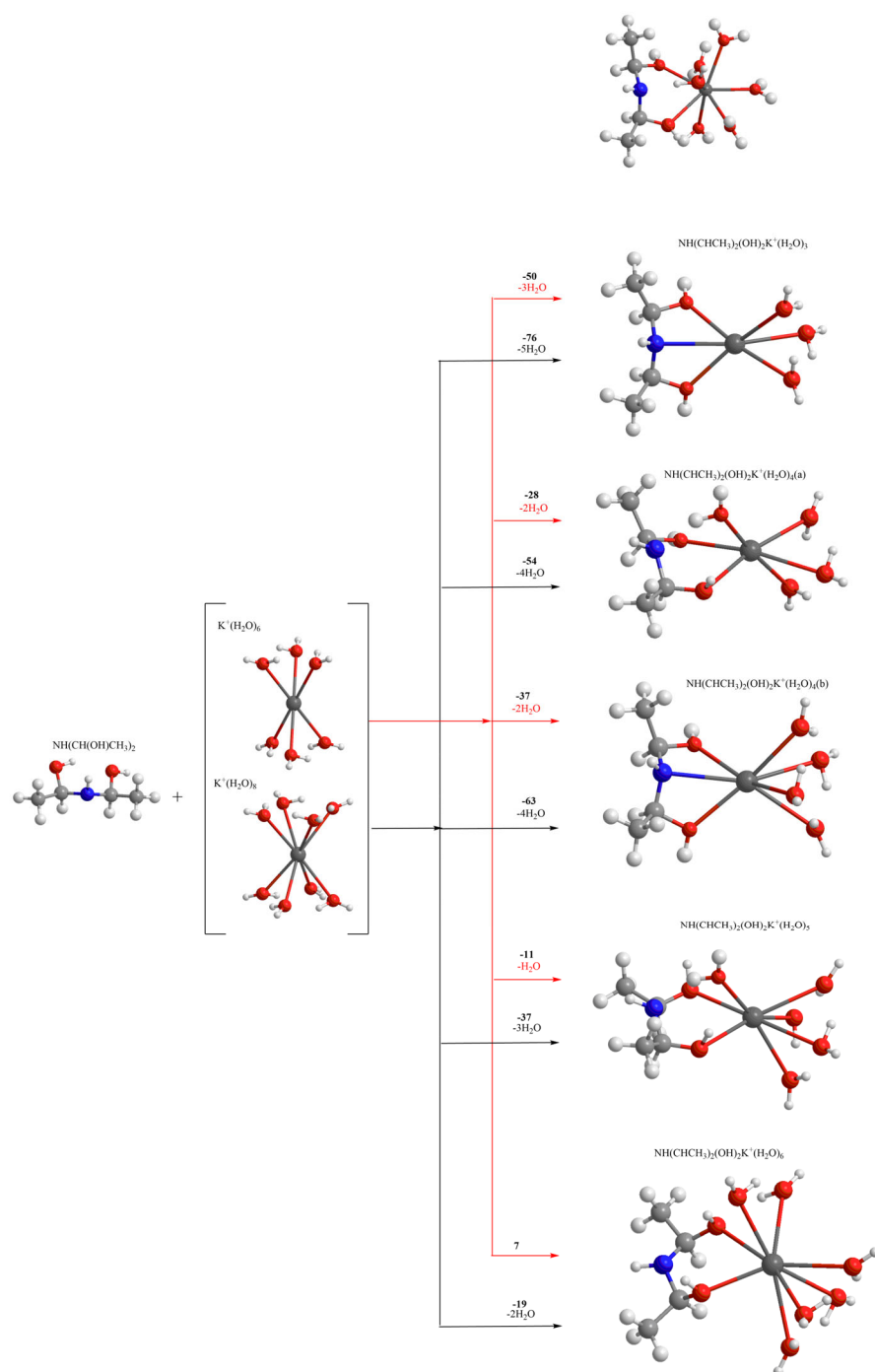


Figure S19. Free energies of reaction for K^+ chelation by 1-(1-hydroxyethylamino)ethanol (3**).** Energies of substitution for substitution of two or three water ligands for 1-(1-hydroxyethylamino)ethanol (**3**) in hexahydrate and octahydrate K^+ complexes were calculated at the ω B97X-D/6-311G(d,p) level employing SCRF SMD modeling in aqueous solution at 298.15 K.

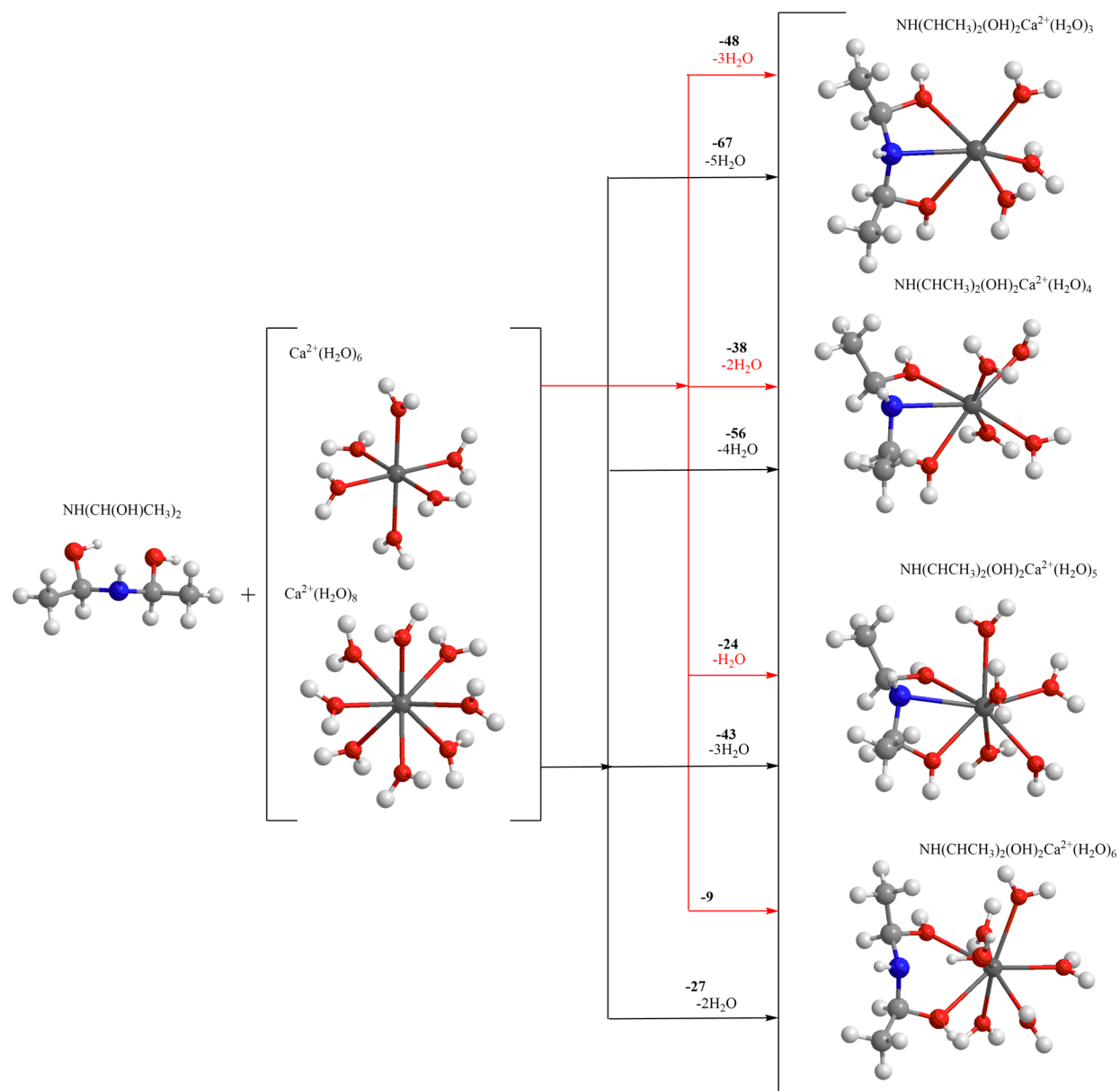


Figure S20. Free energies of reaction for Ca^{2+} chelation by 1-(1-hydroxyethylamino)ethanol (3). Energies of substitution for substitution of two or three water ligands for 1-(1-hydroxyethylamino)ethanol (**3**) in hexahydrate and octahydrate Ca^{2+} complexes were calculated at the $\omega\text{B97X-D/6-311G(d,p)}$ level employing SCRF SMD modeling in aqueous solution at 298.15 K.

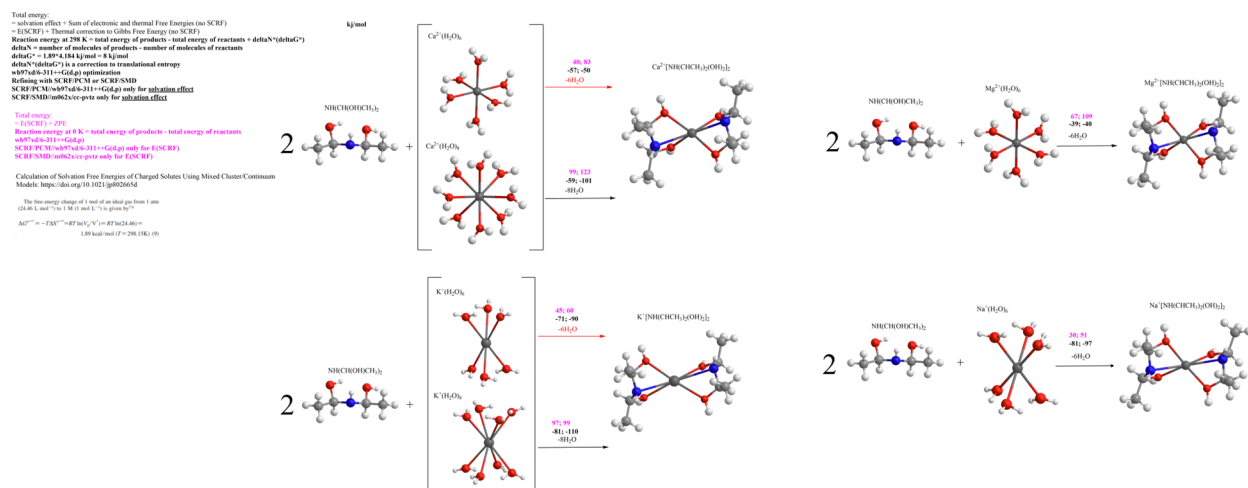


Figure S21. Free energies of reaction for M^{n+} chelation by 1-(1-hydroxyethylamino)ethanol (3). Energies of substitution for substitution of all water ligands for two molecules of 1-(1-hydroxyethylamino)ethanol (3) in hexahydrate Na^+ and Mg^{2+} complexes and hexahydrate and octahydrate K^+ and Ca^{2+} complexes were calculated at the $\omega\text{B97X-D/6-311G(d,p)}$ level employing SCRF SMD modeling in aqueous solution at 298.15 K.

Table S1. Ices studied in this experiment containing acetaldehyde and ammonia or their isotopomers. The ratio of the concentration of the components, ice thickness, and photon energy used are listed.

Experiment	Composition	Ratio	Thickness (nm)	Photon energy (eV)
1	NH ₃ :CH ₃ CHO	2.1 ± 0.7 : 1	2500 ± 250	-
2	ND ₃ :CH ₃ CHO	2.4 ± 1.5 : 1	1800 ± 250	-
3	NH ₃ :CD ₃ CDO	2.9 ± 1.5 : 1	1900 ± 250	-
4	ND ₃ :CD ₃ CDO	1.8 ± 0.8 : 1	2500 ± 250	-
5	NH ₃ :CH ₃ CHO	1.6 ± 0.7 : 1	750 ± 50	10.49
6	NH ₃ : ¹³ CH ₃ ¹³ CHO	1.9 ± 0.7 : 1	750 ± 50	10.49
7	NH ₃ :CD ₃ CHO	1.5 ± 0.6 : 1	750 ± 50	10.49
8	NH ₃ :CD ₃ CDO	1.9 ± 0.7 : 1	750 ± 50	10.49
9	NH ₃ :CH ₃ CHO	2.6 ± 0.4 : 1	750 ± 50	9.93
10	NH ₃ :CD ₃ CDO	2.5 ± 0.6 : 1	750 ± 50	9.93
11	NH ₃ :CD ₃ CDO	1.3 ± 0.5 : 1	750 ± 50	9.50
12	NH ₃ :CH ₃ CHO	2.0 ± 0.5 : 1	750 ± 50	9.30
13	NH ₃ :CD ₃ CDO	2.2 ± 0.5 : 1	750 ± 50	8.90
14	NH ₃ :CH ₃ CHO	2.3 ± 0.5 : 1	750 ± 50	8.90
15	NH ₃ :CH ₃ CHO	1.7 ± 0.6 : 1	750 ± 50	8.10

Table S2. Infrared absorption features observed in ammonia–acetaldehyde ices without isotopic substitution and with $^{13}\text{C}_2$, d_3 , and d_4 isotopically substituted acetaldehyde.

ammonia– acetaldehyde	ammonia– acetaldehyde- $^{13}\text{C}_2$	ammonia– acetaldehyde- d_3	ammonia– acetaldehyde- d_4	Assignment ^{8,22}
5003	5000	5002	5004	ammonia $\nu_1 + \nu_4$
4470	4472	4472	4473	ammonia $\nu_1 + \nu_2$
3372	3374	3375	3368	ammonia ν_3
3271	3267	3272	3269	ammonia $2\nu_4$
3211	3210	3212	3211	ammonia ν_1
-	-	2857	2255	acetaldehyde $2\nu_5$
3001	2990	2753	2218	acetaldehyde ν_1
2962	2951	2226	2181	acetaldehyde ν_{11}
2912	2908	2252	2136	acetaldehyde ν_2
2862	2849	2279	-	acetaldehyde $2\nu_6$
2764	2749	2119	2104	acetaldehyde ν_3
-	-	2195	-	acetaldehyde ²³ $\nu_6 + \nu_7$
-	-	2087	-	acetaldehyde ²³ $\nu_6 + \nu_9$
-	-	-	2068	acetaldehyde $2\nu_{12}$
-	-	1900	-	acetaldehyde ²³ $\nu_6 + \nu_9$
1770	1736	-	-	acetaldehyde $2\nu_9$
1716	1667	1703	1709	acetaldehyde ν_4
-	-	-	1693	acetaldehyde $\nu_8 + \nu_9$
1637	1634	1632	1635	ammonia ν_4
1425	1424	1396	1159	acetaldehyde ν_5
-	-	1139	-	acetaldehyde ²³ ν_6
1348	1338	1026	-	acetaldehyde ν_7
1126	1100	965	1019	acetaldehyde ν_8
1078	1076	1076	1076	ammonia ν_2

Table S3. Infrared band positions of 1-aminoethanol in an acetaldehyde – ammonia ice observed during TPD between 130 and 160 K. Assignment labels: stretching (ν), bending (δ), rocking (ρ), inversion (ω).

Observed Position (cm ⁻¹)	Reported Position (cm ⁻¹) ²⁰	Assignment ²¹	A (10 ⁻¹⁸ cm mol ⁻¹)
3354	3347	$\nu_{asym}(\text{NH})$	9.9 ± 2.0
3286	3258	$\nu_{sym}(\text{NH})$	3.5 ± 0.7
3203	-	comb./overtone	0.37 ± 0.07
3190	-	$\nu(\text{OH})$	130 ± 30
2986	2978	$\nu(\text{CH}_3)$	6.7 ± 1.3
2935	2934	$\nu(\text{CH}_3)$	3.2 ± 0.6
2879	2865	$\nu(\text{CH}_3)$	13 ± 3
2773	-	$\nu(\text{CH})$	6.1 ± 1.2
2707	-	$\nu(\text{CH})$	15 ± 3
1630	1616	$\delta(\text{NH})$	6.9 ± 1.4
1400	1453	$\delta(\text{CH})$	0.63 ± 0.13
1394	-	$\delta(\text{CH})$	25 ± 5
1375	1374	$\delta(\text{CH})$	1.4*
1346	1334	$\delta(\text{CH})/\delta(\text{OH})$	9.9 ± 2.0
-	1244	$\rho(\text{NH})$	1.9*
1176	-	$\nu(\text{CO})/\nu(\text{CN})$	6.9 ± 1.4
1132	1134	$\nu(\text{CO})/\nu(\text{CN})$	6.8 ± 1.4
1101	1101	$\nu(\text{CN})/\nu(\text{CC})$	10*
1068	-	$\nu(\text{CN})/\nu(\text{CC})$	6.9 ± 1.4
993	-	-	16 ± 3
933	925	$\nu(\text{CO})/\nu(\text{CN})$	12*
860	-	$\omega(\text{NH}_2)$	13 ± 3

Table S4. Four-wave mixing schemes employed to generate vacuum ultraviolet (VUV) photons for photoionization in experiments 2 – 12. With the exception of 10.49 eV photons all experiments use at least one dye laser pumped by a neodymium yttrium-aluminum garnet (Nd:YAG) laser harmonic (355 or 532 nm) appropriate for the dye in use.

Experiments	Medium	$\omega_{\text{VUV}} =$	ω_1 (nm)	ω_1 Dye	ω_2 (nm)	ω_2 Dye	Energy (eV)
5 – 8	Xenon	$3\omega_1$	355 ^a	-	-	-	10.49
9, 10	Krypton	$2\omega_1 - \omega_2$	202.316	Rhodamine 610/640	532 ^a	-	9.93
11	Krypton	$2\omega_1 - \omega_2$	202.316	Rhodamine 610/640	449.8	Coumarin 450	9.50
12	Xenon	$2\omega_1 - \omega_2$	222.566	Coumarin 450	673.4	LDS 698	9.30
13, 14	Xenon	$2\omega_1 - \omega_2$	222.566	Coumarin 450	553.2	Pyrromethene 580	8.90
15	Xenon	$2\omega_1 - \omega_2$	249.628	Coumarin 503	676.2	LDS 698	8.10

^a Nd:YAG harmonic

References

- (1) Abplanalp, M. J., Förstel, M., and Kaiser, R. I. (2016). Exploiting Single Photon Vacuum Ultraviolet Photoionization to Unravel the Synthesis of Complex Organic Molecules in Interstellar Ices. *Chem. Phys. Lett.* *644*, 79-98.
- (2) Abplanalp, M. J., Gozem, S., Krylov, A. I., Shingledecker, C. N., Herbst, E., and Kaiser, R. I. (2016). A Study of Interstellar Aldehydes and Enols as Tracers of a Cosmic Ray-Driven Nonequilibrium Synthesis of Complex Organic Molecules. *Proc. Natl. Acad. Sci. U.S.A.* *113*, 7727-7732.
- (3) Jones, B. M. and Kaiser, R. I. (2013). Application of Reflectron Time-of-Flight Mass Spectroscopy in the Analysis of Astrophysically Relevant Ices Exposed to Ionization Radiation: Methane (CH₄) and D₄-Methane (CD₄) as a Case Study. *J. Phys. Chem. Lett.* *4*, 1965-1971.
- (4) Maity, S., Kaiser, R. I., and Jones, B. M. (2014). Infrared and Reflectron Time-of-Flight Mass Spectroscopic Study on the Synthesis of Glycolaldehyde in Methanol (CH₃OH) and Methanol–Carbon Monoxide (CH₃OH–CO) Ices Exposed to Ionization Radiation. *Faraday Discuss.* *168*, 485-516.
- (5) Turner, A. M., Abplanalp, M. J., Chen, S. Y., Chen, Y. T., Chang, A. H. H., and Kaiser, R. I. (2015). A Photoionization Mass Spectroscopic Study on the Formation of Phosphanes in Low Temperature Phosphine Ices. *Phys. Chem. Chem. Phys.* *17*, 27281-27291.
- (6) Hudson, R. L., Yarnall, Y. Y., and Gerakines, P. A. (2022). Infrared Spectral Intensities of Amine Ices, Precursors to Amino Acids. *Astrobiol.* *22*, 452-461.
- (7) Hudson, R. L. and Coleman, F. M. (2019). Infrared Intensities and Molar Refraction of Amorphous Dimethyl Carbonate – Comparisons to Four Interstellar Molecules. *Phys. Chem. Chem. Phys.* *21*, 11284-11289.
- (8) Bouilloud, M., Fray, N., Bénilan, Y., Cottin, H., Gazeau, M. C., and Jolly, A. (2015). Bibliographic Review and New Measurements of the Infrared Band Strengths of Pure Molecules at 25 K: H₂O, CO₂, CO, CH₄, NH₃, CH₃OH, HCOOH and H₂CO. *Mon. Not. R. Astron. Soc.* *451*, 2145-2160.
- (9) Kleimeier, N. F., Eckhardt, A. K., and Kaiser, R. I. (2020). A Mechanistic Study on the Formation of Acetic Acid (CH₃COOH) in Polar Interstellar Analog Ices Exploiting Photoionization Reflectron Time-of-flight Mass Spectrometry. *Astrophys. J.* *901*, 84.
- (10) *Gaussian 09, Revision D.01*; Gaussian, Inc.: Wallingford CT, 2013. (accessed).
- (11) Montgomery, J. A., Frisch, M. J., Ochterski, J. W., and Petersson, G. A. (1999). A Complete Basis Set Model Chemistry. VI. Use of Density Functional Geometries and Frequencies. *J. Chem. Phys.* *110*, 2822-2827.

- (12) Montgomery, J. A., Frisch, M. J., Ochterski, J. W., and Petersson, G. A. (2000). A Complete Basis Set Model Chemistry. VII. Use of the Minimum Population Localization Method. *J. Chem. Phys.* *112*, 6532-6542.
- (13) Chai, J. D. and Head-Gordon, M. (2008). Long-Range Corrected Hybrid Density Functionals With Damped Atom-Atom Dispersion Corrections. *Phys. Chem. Chem. Phys.* *10*, 6615-6620.
- (14) Marenich, A. V., Cramer, C. J., and Truhlar, D. G. (2009). Universal Solvation Model Based on Solute Electron Density and on a Continuum Model of the Solvent Defined by the Bulk Dielectric Constant and Atomic Surface Tensions. *J. Phys. Chem. B* *113*, 6378-6396.
- (15) Streitferdt, V., Tiefenthaler, S. M., Shenderovich, I. G., Gärtner, S., Korber, N., and Gschwind, R. M. (2021). NMR-Spectroscopic Detection of an Elusive Protonated and Coinage Metalated Silicide $[\text{NHC}^{\text{Dipp}}\text{Cu}(\eta^4\text{-Si}_9\text{H})]^{2-}$ in Solution. *Eur. J. Inorg. Chem.* *2021*, 3684-3690.
- (16) Smyth, C. P. and Hitchcock, C. S. (2002). The Dielectric Constants and Transitions of Solid Ammonia, Hydrogen Sulfide and Methyl Alcohol. *J. Am. Chem. Soc.* *56*, 1084-1087.
- (17) Zhao, Y. and Truhlar, D. G. (2008). Density Functionals With Broad Applicability in Chemistry. *Acc. Chem. Res.* *41*, 157-167.
- (18) Dunning, T. H. (1989). Gaussian Basis Sets for Use in Correlated Molecular Calculations. I. The Atoms Boron Through Neon and Hydrogen. *J. Chem. Phys.* *90*, 1007-1023.
- (19) Bryantsev, V. S., Diallo, M. S., and Goddard, W. A., 3rd. (2008). Calculation of Solvation Free Energies of Charged Solutes Using Mixed Cluster/Continuum Models. *J. Phys. Chem. B* *112*, 9709-9719.
- (20) Duvernay, F., Dufaure, V., Danger, G., Theulé, P., Borget, F., and Chiavassa, T. (2010). Chiral Molecule Formation in Interstellar Ice Analogs: Alpha-Aminoethanol $\text{NH}_2\text{CH}(\text{CH}_3)\text{OH}$. *Astron. Astrophys.* *523*, A79.
- (21) Chen, L. N. and Woon, D. E. (2011). A Theoretical Investigation of the Plausibility of Reactions between Ammonia and Carbonyl Species (Formaldehyde, Acetaldehyde, and Acetone) in Interstellar Ice Analogs at Ultracold Temperatures. *J. Phys. Chem. A* *115*, 5166-5183.
- (22) Kleimeier, N. F. and Kaiser, R. I. (2021). Interstellar Enolization-Acetaldehyde (CH_3CHO) and Vinyl Alcohol ($\text{H}_2\text{CCH}(\text{OH})$) as a Case Study. *ChemPhysChem* *22*, 1229-1236.
- (23) Kleimeier, N. F., Eckhardt, A. K., Schreiner, P. R., and Kaiser, R. I. (2020). Interstellar Formation of Biorelevant Pyruvic Acid (CH_3COCOOH). *Chem* *6*, 3385-3395.